

Evidence for multiple Liquid-liquid phase transitions in carbon, and the Friedel-ordering of its liquid state.

M.W.C. Dharma-wardana* and Dennis D. Klug.

National Research Council of Canada, Ottawa, Canada, K1A 0R6

(Dated: January 28, 2022)

Abstract

Carbon, the fourth most abundant element in the Universe forms a metallic fluid with transient covalent bonds on melting. Its liquid-liquid phase transitions, intensely sought using simulations had been elusive. Here we use density functional theory (DFT) simulations with up to 108 atoms using molecular dynamics, as well as one-atom DFT as implemented in the neutral pseudo-atom method where multi-atom effects are treated by ion-ion correlation functionals. Both methods use electron-electron exchange correlation functionals for electron many-body effects. Here we show using both methods, that liquid carbon displays multiple liquid-liquid transitions linked to changes in coordination number in the density range 3 g/cm^3 , to $\sim 6 \text{ g/cm}^3$ when a coordination number of 12 is reached. The transitions disappear by 4 eV in temperature. The calculated pressures and transition densities are shown to be sensitive to the exchange-correlation functionals used. Significantly, we find that a simple metallic model yields the structure factors and thermodynamics with quantitative accuracy, without invoking any covalent-bonding features. The ion-ion structure factor for these densities and temperatures is found to have a subpeak tied to twice the Fermi wavevector, constraining the fluid in momentum space. The dominant Friedel oscillations forming the pair interactions correlate the ions and drive the multiple liquid-liquid phase transitions. Our results suggest that liquid carbon typifies a class of fluids whose structure is ordered by the long-ranged Friedel oscillations in the pair-potentials. These results are critical to terrestrial and astrophysical studies, inertial fusion using carbon drivers, refined shock experiments, and in seeking new carbon-based materials.

PACS numbers: 52.25.Jm, 52.70.La, 71.15.Mb, 52.27.Gr

* Email address: chandre.dharma-wardana@nrc-cnrc.gc.ca

I. INTRODUCTION

The physics and chemistry of carbon is central to the evolution of stars, exoplanets as well as the earth, comets even in the context of interstellar dust. Hull *et al* [1] have recently emphasized the importance of studying *l*-carbon in many chemical physics contexts, while Lazicki *et al* [2] find persisting diamond structures even at terapascal pressures. Carbon plays crucial roles in many industrial processes, and in frontier research into new carbon materials. It is used for encapsulating deuterium in inertial laser fusion. Its properties in the regime of warm-dense matter have been intensely studied. Intriguingly, although metallic, liquid carbon (*l*-carbon) shows covalent bonding characteristics and most theoretical studies have attempted a detailed account of such interactions that contain directional, orientational and other poly-atomic molecular features, using expensive computations involving hundreds of atoms [3–5].

While phase transitions in solids involve changes in symmetry or some ‘order parameter’ of a property like magnetism, liquid-liquid phase transitions (LPTs) typically show a discontinuity or divergence in a thermodynamic property like the pressure, or the compressibility. Such LPTs may be caused by changes in short-ranged bonding effects, long-ranged non-directional many-body correlations or ‘volume forces’.

Carbon [3, 6] silicon, and germanium etc., are ‘tetrahedral fluids’ that are metallic with four free electrons per ion in the range of densities studied here. Supercooled liquid silicon (*l*-Si) undergoes a subtle structural liquid-liquid transition [7]. Simulations of *l*-Si in thermal equilibrium show other LPTs as well [8]. At higher densities, in analogy with LPTs found in alkali metals [9], free electron phases, electrone etc., may also exist [10]. Although a transient covalent-bonding picture is popular in interpreting results from density functional theory (DFT) and molecular dynamics (MD) simulations, here we show that a simple metallic picture quantitatively accounts for the structure and thermodynamics of *l*-carbon, just as for *l*-Si. The metallic picture treats long-ranged Friedel oscillations and ionic interactions accurately, exposing hitherto elusive LPTs generic to this class of fluids.

LPTs in carbon were discussed by van Thiel *et al* [11], while Glosli *et al* [12] used the multi-center empirical ‘Brenner’ potential and found a single LPT involving changes in bonding and coordination. However, a DFT-MD study using the Perdew-Burke-Ernzerhof (PBE) exchange-correlation (xc) functional [13] found no such LPT [14]. Kraus *et al* [15] also

found empirical potentials to be unreliable and used N -atom density functional calculations coupled to MD simulations in their laser-shock experiments on carbon.

Kraus *et al* state that “Simple potentials from fluid theory like that of Lennard and Jones fail as well. We have also tested combinations of screened Coulomb interactions and Lennard-Jones-type interactions. All of these calculations always predict a first peak around $k=4.3 \text{ \AA}^{-1}$ or a correlation length of 1.45 \AA which is related to the mean density of the sample. However, the measured data do not support such a structure factor. On the other hand, the observed structure factors agree very well with results from DFT-MD simulations. Such simulations include the full quantum nature of the electrons and, thus, go far beyond simple pair interactions between the nuclei. In particular, they are able to describe short-time bonding”.

While *ad hoc* simple ‘screened Coulomb interactions’ do fail [16], we show in this study (see also Ref. [6]) that properly constructed pseudopotentials and pair-potentials based on linearly screened Coulomb interactions built on rigorous first principles methods give quantitative agreement with multi-center DFT-MD calculations for l -carbon, *without* the need for multi-center potentials.

Here we use two independent DFT methods to establish hitherto unexpected multiple LPTs linked to changes in coordination number at the densities studied. Unlike in previous studies, we have examined the compressibility of liquid carbon on very fine grids of densities along several isotherms to expose the presence of discontinuities in the compressibility, while similar studies for l -aluminum in a corresponding density range show no such discontinuities, as expected for aluminum.

Since the melting point of diamond is $\sim 0.5 \text{ eV}$ in energy units of temperature T used here, we study the range $T = 1 - 10 \text{ eV}$. Such systems are conveniently experimentally studied using short-pulse lasers [2, 15]. We show that l -carbon is typical of a class of fluids (e.g., C, Si, Ge) whose structure is determined by strong electron scattering across the Fermi surface, with a momentum transfer of $2k_F$, where k_F is the Fermi wavevector.

While a fluid cannot support a static charge density wave, the short-ranged structure of the fluid can get modified. Here it produces a peak at $2k_F$ by splitting the main peak in the structure factor $S(k)$. This mechanism creates LPTs not found in other metallic liquids like l -aluminum where the compressibility shows no discontinuities in the relevant density range. This suggests a new class of momentum-constrained *Friedel ordered* fluids associated

with strong $2k_F$ scattering. Highly refined shock-wave experiments may expose these subtle LPTs.

II. DENSITY FUNCTIONAL METHODS USED IN THE STUDY

The DFT methods used here are discussed briefly in the Appendix. The DFT-MD method implemented in VASP [17] or ABINIT [18] uses N atoms in the simulation cell, typically with $N \sim 100 - 500$. It is referred to as ‘Quantum MD’ (QMD) here, and was used recently to study l -carbon by Vorberger *et al.*, [5] where the Perdew-Burke- Ernzerhof (PBE) [13] xc-functional at $T=0$ was used to treat electron-electron many-body effects. Such multi-center densities are found to be sensitive to the xc-functional used [19]. Thus results for l -Si from the PBE functional differed significantly from those of the ‘strongly constrained and appropriately normed’ (SCAN) functional [20]. In our work we have used the SCAN functional for N -atom QMD carbon simulations via the VASP code in this study. The sensitivity to the number of atoms N used in the simulation is investigated using QMD calculations for $N = 64$ and 108.

The very heavy computational effort in N -atom QMD approaches can be removed while still retaining the power and rigour of DFT in a properly formulated full one-body DFT where $N = 1$. According to Hohenberg and Kohn, *one-body* densities of electrons and ions completely determine the thermodynamics of *any* arbitrary electron-ion system. Hence, in principle, N -atom DFT with $N=1$ should provide accurate results if multi-ion effects could be handled by a suitable ion-ion xc-functional in addition to the usual electron-electron xc-functional. Such a one-atom DFT is utilized in the neutral pseudoatom (NPA) method used here [8, 21]. Its accuracy has been established by many previous calculations [8, 22] of static as well as dynamic properties [23]. The many-ion and many-electron effects are included in one-atom DFT via exchange-correlation (xc) functionals for electrons as well as for ions (see Appendix).

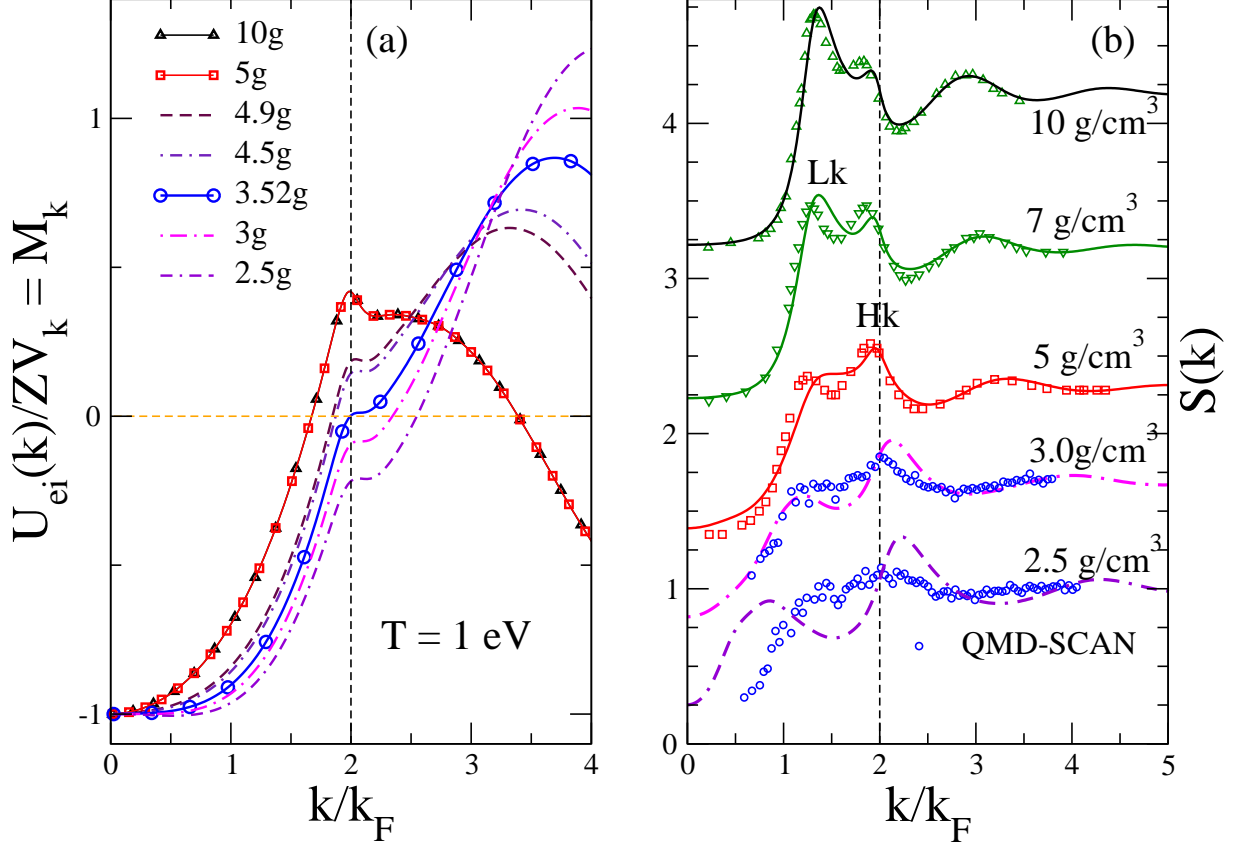


FIG. 1. (Colour online) Pseudopotentials and structure factors. (a) The LR-NPA pseudopotential $U_{ei}(k)$ for l -carbon at 1 eV for $2.5 \text{ g/cm}^3 \leq \bar{\rho} \leq 10 \text{ g/cm}^3$. The U_{ei} is invariant between 5-10 g/cm^3 ; a sharp change occurs below 5 g/cm^3 . The $U_{ei}(k = 2k_F) \rightarrow 0$ at $\rho_D \simeq 3.5 \text{ g/cm}^3$ (line with circles). (b) shows typical $S(k)$ using the LR- $U_{ei}(k)$ and the electron response function $\chi_{ee}(k, T, \bar{n})$. The unconnected symbols for $\bar{\rho} \geq 5 \text{ g/cm}^3$ are the QMD $S(k)$ of Ref. [5] using the PBE functional. The smooth curves are NPA calculations. The high- k subpeak (marked Hk) falls on $2k_F$ for $\bar{\rho} \geq 3 \text{ g/cm}^3$. We compare the LR-NPA $S(k)$ and QMD-SCAN $S(k)$ at 3 g/cm^3 , and 2.5 g/cm^3 showing the failure of LR below 3 g/cm^3 .

III. THE PSEUDOPOTENTIALS AND PAIR-POTENTIALS GENERATED FROM THE NPA

The all-electron NPA calculation self-consistently generates the Kohn-Sham one-body electron charge distribution (see Appendix) around a carbon nucleus placed in the appropriate environment in the fluid. This charge distribution is used to construct a pseudopotential which is then employed to construct a pair-potential. If a metallic model with strong screen-

ing is assumed, the above steps can be carried out within linear response (LR) theory. Let the free electron density around the ion of average charge \bar{Z} be denoted by $n_f(r)$, while the average (uniform) free electron density in the fluid is denoted by \bar{n} . In our case $\bar{Z} = 4$. We use the free-electron charge pileup $\Delta n_f(r) = n_f(r) - \bar{n}$ and its Fourier transform $\Delta n_f(k)$ to construct the electron-ion pseudopotential, in Hartree atomic units,

$$U_{ei}(k) = \Delta n_f(k) / \chi(k, r_s, T) \quad (1)$$

$$= -\bar{Z}V_k M_k, \quad V_k = 4\pi/k^2. \quad (2)$$

Here $\chi(k, r_s, T)$, abbreviated to $\chi(k)$ is the fully interacting finite-temperature response function of the uniform electron fluid at the density \bar{n} associated with the electron Wigner-Seitz radius r_s . The details of the calculation of $\chi(k)$ as well as the limitations of this pseudopotential are discussed in the Appendix. Here we note that a full electron non-linear DFT calculation has been applied to the electron-nuclear interaction in obtaining $\Delta n_f(r)$, and LR is used only in defining a pseudopotential. Thus the pseudopotential incorporates the non-linear aspects of the Kohn-Sham calculation contained in the NPA model.

The pseudopotential $U_{ei}(k)$ is re-expressed in terms of the point-ion potential $\bar{Z}V_k$ and the form factor M_k which is unity only for a point ion. This is a simple local (*s*-wave) potential and we have found it adequate for quantitatively reproducing results obtained from complex *N*-atom QMD using advanced non-local pseudopotentials for a variety of materials. The resulting pseudopotentials are shown in panel (a) of figure 1.

The pair-potential within linear response that results from Eq. 1 is, in Hartree atomic units:

$$V_{ii}(k) = Z^2 V_k + |U_{ei}(k)|^2 \chi(k). \quad (3)$$

Its *r*-space form is obtained by Fourier transformation, and hence the calculation of pseudopotentials and pair-potentials from the NPA within LR is very simple, rapid and provides first-principles results. The ion-ion LR pair potential $V_{ii}(r)$ will be denoted by $V(r)$ for simplicity, where needed.

The *N*-center QMD calculation provides an *N*-center potential energy surface. This may be used to construct force-matched pair-potentials [16, 24]. A typical comparison is shown in Fig. 2. The electrons have been eliminated from such potentials which require three-center (and higher) terms in the total energy. In contrast, the NPA retains contributions from the

two-component system of free electrons and ions, pair-interactions and their xc-contributions to the free energy.

With $Z = 4$, *l*-carbon is a dense electronically degenerate metal even at 1 eV, even for 2.5 g/cm^3 when $E_F \simeq 23 \text{ eV}$. Hence electron-ion scattering occurs essentially at the Fermi energy E_F , with a momentum transfer $q = 2k_F$, where k_F is the Fermi momentum. The form-factor M_k changes sharply near 5 g/cm^3 as seen from Fig. 1(a). Then, near the ‘diamond density’ ρ_D , viz., $\simeq 3.52 \text{ g/cm}^3$ M_k at $k = 2k_F$ passes through zero and changes sign (curve with circles). So at ρ_D , when $U_{ei}(k = 2k_F)$ becomes zero the pair potential becomes just $Z^2V_{k_F}$. Then the pair potential is that of two *unscreened* point-like carbon ions, and interact strongly. Both NPA and QMD methods find a first-order LPT very near this density.

The NPA structure factors $S(k)$ displayed in Fig. 1 are in good agreement with the QMD data, showing the split-peak structure etc., but become less satisfactory at lower densities, i.e., below ρ_D and certainly below 3 g/cm^3 , at 1 eV. Stanek *et al* [16] showed this explicitly in their study of NPA pair potentials at the graphite density. This is consistent with the fact that linear-response methods are known to become unsatisfactory for expanded metals.

IV. STRONG $2k_F$ SCATTERING AND THE FRIEDEL STRUCTURING OF THE FLUID

The ion distribution $\rho(r) = \bar{\rho}g(r)$ is given by the NPA-DFT equation (see Appendix) for ions which are classical. It uses the pair-potential $V_{ii}(r)$ and an ion-ion xc-functional based on hyper-netted chain (HNC) diagrams [25]. This amounts to solving a HNC equation [25] using the NPA pair potential to yield the $g(r)$ and the $S(k)$ of the ion subsystem. In Fig. 1(b) we compare the results from the NPA, and QMD [5] where the PBE xc-functional ($T = 0$) was used. The first peak of $S(k)$ displays lower- k (Lk) and higher- k (Hk) subpeaks.

The inter-particle interactions are dominated by electron-ion interactions causing strong electron scattering from one edge of the Fermi surface to the opposite edge, with a momentum transfer of $q = 2k_F$ as the fluid is essentially degenerate since T/E_F is small. In a solid this could have spawned a charge-density wave with the period $2k_F$. The fluid responds by creating the high- k peak Hk as close to $2k_F$ as possible for densities in the range $10 \text{ g/cm}^3 \geq \bar{\rho} \geq 3 \text{ g/cm}^3$, as shown in Fig. 1(b).

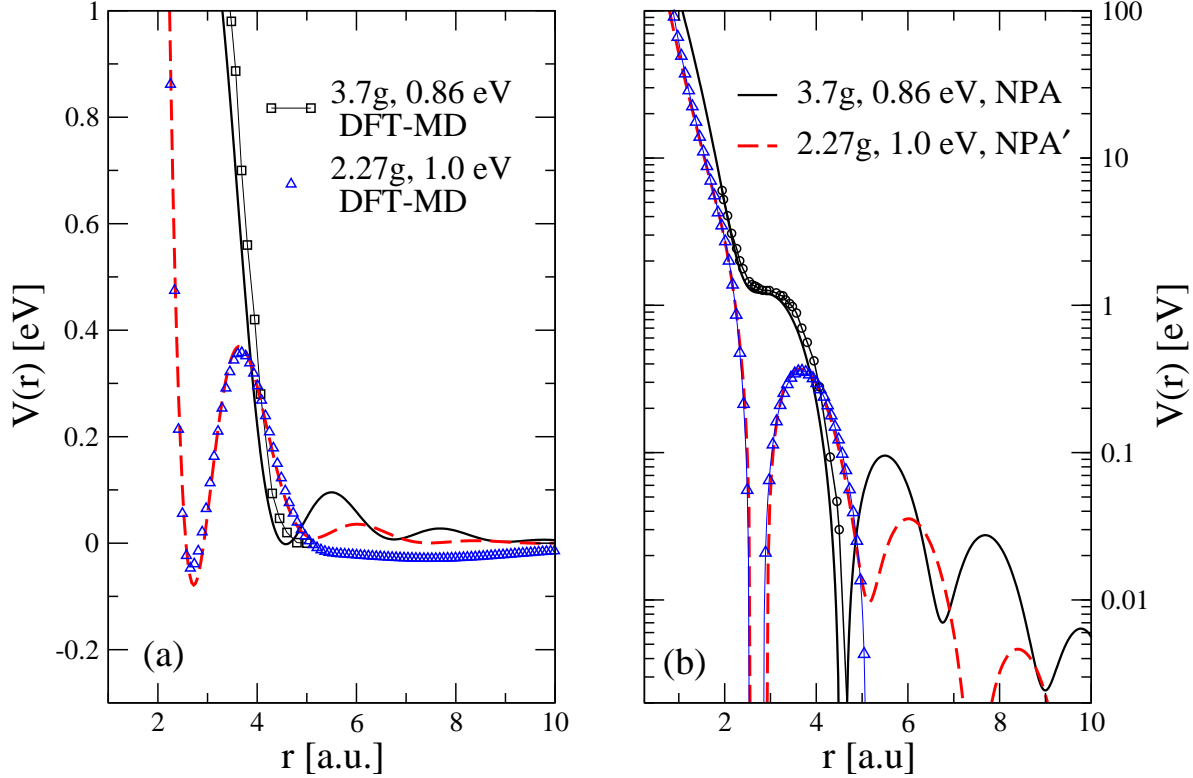


FIG. 2. (Color online) The C-C pair potentials from a 64-atom force-matched QMD calculation and from the NPA. (a) The QMD potential at $\bar{\rho}=3.27 \text{ g/cm}^3$ [24] compared with the NPA linear-response pair potential. The QMD potential from the $N=64$ simulation fails to recover the higher Friedel oscillations (for $r > 5 \text{ a.u.}$) seen in the NPA potentials and may not capture long-range correlations relevant to phase transitions. (b) The same data on a log-y scale. The maximum of the $g(r)$ at this density corresponds to the positive energy ledge for this range of densities.

The electron xc-energy favours a high-density electron fluid even if it requires positioning ions in a positive energy ledge of the pair-potential (e.g., Fig. 2). This is less advantageous at lower density and the peak Hk at $2k_F$ grows at the expense of Lk, as seen in Fig. 1(b). Scattering from atoms positioned in the Friedel minima need to contribute coherently to form the subpeak Hk in $S(k)$ at $2k_F$. This coherence links the coordination number with the liquid phases of the fluid and their LPTs.

The ion distribution modifies itself to minimize the energy of the system in two ways: (i) its Hk peak locates itself as closely as possible to $2k_F$. (ii) At densities below ρ_D , the first atomic shell attempts to continue to retain a high coordination number N_c at the expense of outer shells. Even when $\bar{\rho}$ is low, the *local density* of the fluid adjusts to bring Hk to $2k_F$,

lowering the free energy via strong scattering at E_F . That is, atoms may be drawn towards the central ion by decreasing the depths of secondary Friedel minima. This is evidenced by the nature of the pair-potentials at different density regimes, as discussed in Sec. VI.

The split structure of the first peak of the structure factor of liquid carbon, liquid silicon [8] and liquid germanium [6, 26] arise from similar physics. Thus we may consider liquid carbon to be a prototype of a class of liquids whose ionic structure has momentum ordering due to strong $2k_F$ scattering and reflects the $2k_F$ periodicity of the Friedel oscillations in the pair-potentials.

The structure of momentum-correlated fluids like l -C, l -Si and l -Ge is already tightly linked by the strong $2k_F$ scattering at the Fermi energy, and further adjustment to how the atoms are packed in the fluid by, say, bridge-diagram corrections is hardly possible. Thus the structure factors and derived properties like the pressure are quite insensitive to bridge corrections [26]. This is in contrast to ‘normal’ metallic fluids like l -Al where the bridge corrections are important enough to modify the pressure and the compressibility.

Simulations using QMD do not use an ion-ion xc-functional, but use a large number of atoms to build the ionic correlations through explicit interactions. They reveal the existence of transient microscopic “bonding” which may be the real-space *dynamic* manifestation of the $2k_F$ correlations in momentum space that seem to occur in this class of fluids with Friedel ordering, leading to a $2k_F$ subpeak in $S(k)$.

V. LPTS IN LIQUID CARBON

The LPTs are evidenced by the discontinuities in the pressure and the compressibility obtained from the NPA. We first make a series of calculations on a finely spaced set of points in density along an isotherm using the NPA, profiting from the rapidity of NPA calculations. The $k \rightarrow 0$ limit of $S(k)$ is the isothermal compressibility ratio κ/κ_0 , where $\kappa_0 = 1/\bar{\rho}T$ is the ideal (noninteracting) compressibility. Such a determination of κ is independent of the pressure calculation. That is, κ is not determined by taking a density derivative of the pressure, and constitutes an independent determination of LPTs including those that are second order transitions. Unfortunately, such a direct and microscopic determination of $S(k \rightarrow 0)$ is very costly in QMD as the accessible smallest value of k is limited by the inverse of the linear dimension $L \propto N^{1/3}$ of the simulation box.

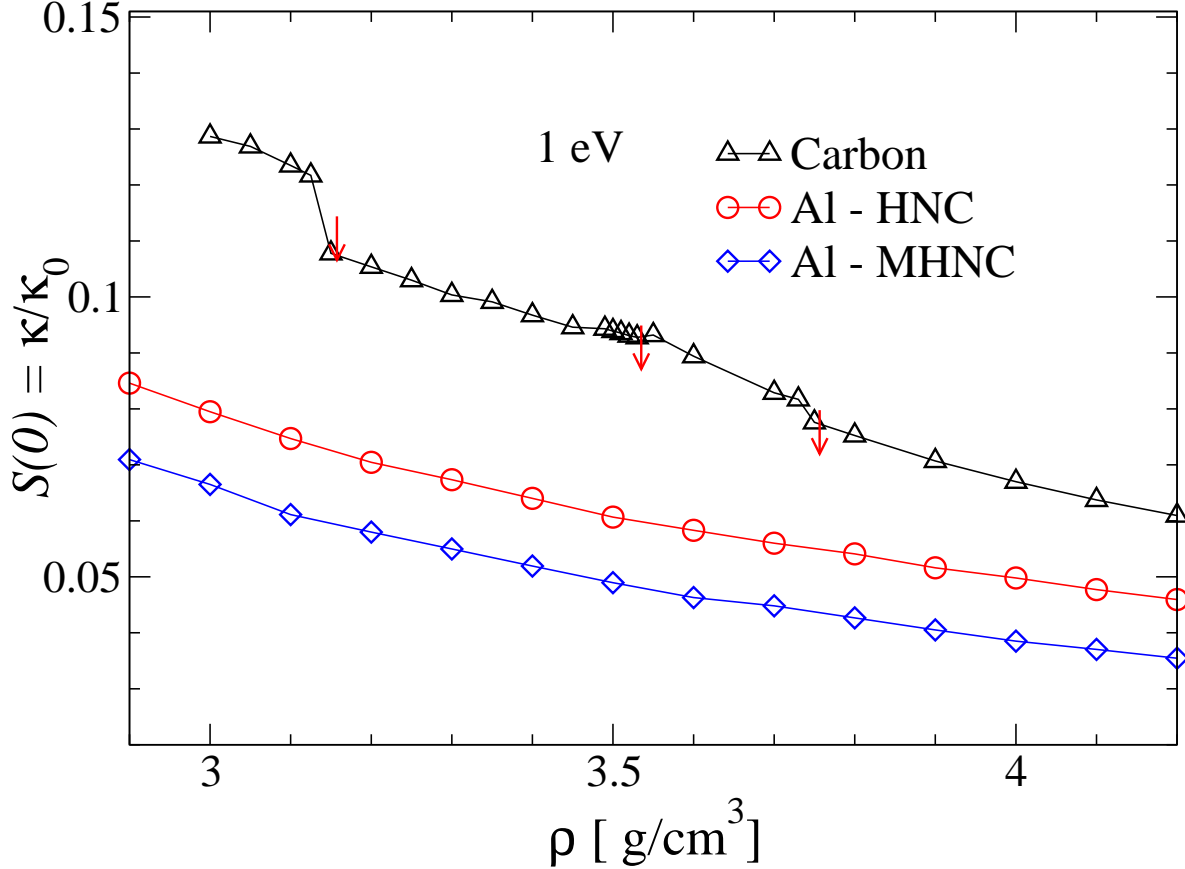


FIG. 3. (Color online) The compressibility ratio κ/κ_0 of *l*-carbon and *l*-aluminum at 1 eV in the range of densities 3-4 g/cm³ from NPA calculations. Their normal densities are, diamond ~ 3.5 g/cm³, and aluminum, 2.7 g/cm³. The structure of *l*-Al is not controlled by strongly correlated $2k_F$ scattering and Friedel-oscillations, and shows no discontinuities associated with changes in coordination number, in contrast to *l*-carbon displaying such discontinuities (short vertical arrows). Bridge corrections modify the $S(0)$ of *l*-aluminum, as shown by the difference in the HNC (without bridge) and MHNC (with bridge) calculations. The $S(0)$ of *l*-carbon remains unchanged for this ρ, T region on inclusion of bridge corrections (see Appendix).

In Fig. 3. We show the compressibility ratio for *l*-carbon as well as for *l*-aluminum for the range ~ 3 -4 g/cm³. Aluminum forms a metallic liquid with $\bar{Z} = 3$ but its structure factor does not show the $2k_F$ splitting seen in *l*-carbon or *l*-silicon, and hence there is no incipient charge-density-wave type of effect. The Friedel ordering which links the coordination and shell filling does not occur in liquid aluminum where the liquid structure is mainly determined by packing effects. This also makes Al sensitive to bridge corrections. Thus HNC

calculations of the $S(0)$ for l -aluminum differs from the result obtained from the modified HNC equation (MHNC) or on using MD. In contrast, the highly Friedel-correlated l -carbon is insensitive to bridge corrections as atomic positions preferably pack into the shells formed by the minima of the Friedel oscillations in the pair-interactions. Unlike l -aluminum, l -carbon shows three discontinuities in this range of densities. We study them in detail below.

In Fig. 4(a) we display the compressibility ratio $S(0)$ and the pressure at 1 eV for a larger range of densities. The compressibility ratio at 2 eV is also shown. The discontinuities are indicated by vertical lines. A selection of the discontinuities are studied further using the vastly more expensive QMD simulations implemented via VASP. The SCAN electron xc-functional at $T = 0$ was used and the results are presented in Fig. 4(b). The use of the $T = 0$ approximation in QMD is quite accurate as T/E_F is 0.035 even at $\bar{\rho} = 3 \text{ g/cm}^3$ at 1 eV. We identify the following discontinuities and label them as follows.

The LPTs are named LPT₃, LPT_{3.5}, LPT_{3.7}, LPT_{4.5} and LPT_{5.3} being at densities 3.15, 3.5, 3.75, 4.5 and 5.3 g/cm³ respectively as given by the NPA calculation. They can be conveniently classified in terms of the coordination number N_c (as estimated from the area under the first peak of the pair-distribution functions) of the regions separated by the LPTs. Beyond the LPT_{5.3} N_c has reached 12 and no further LPTs associated with changes in coordination number are expected. Vorberger *et al* [5] have reported estimates of the coordination number in the relevant density range, and our results are consistent with their N_c estimates. They are indicated in Fig. 4(b) where we have selected the density range $2.9 \text{ g/cm}^3 < \bar{\rho} < 4 \text{ g/cm}^3$ for further detailed study.

Figure 4(a) displays the QMD pressures from Ref. [5], and from our QMD runs using the SCAN functional and 108 atoms. The NPA uses the finite- T xc-functional of Ref. [27] within the local density approximation (LDA). We have compared the finite- T electron xc-functional that we use in the NPA with that of Dornheim *et al* [28, 29], and find excellent agreement in the range of $\bar{\rho}, T$ used here. The LDA is deemed to be adequate because the charge density in the NPA is very simple compared to the complex N -center density used in QMD calculations. The use of ever more complex N -center calculations have led to a ‘‘Jacob’s ladder’’ of ever-more complicated electron xc-functionals that are deployed in QMD.

The pressure estimates from PBE-QMD, SCAN-QMD and the LDA-NPA calculations fall within the differences in the xc-functionals used. The NPA calculates the pressure from a free

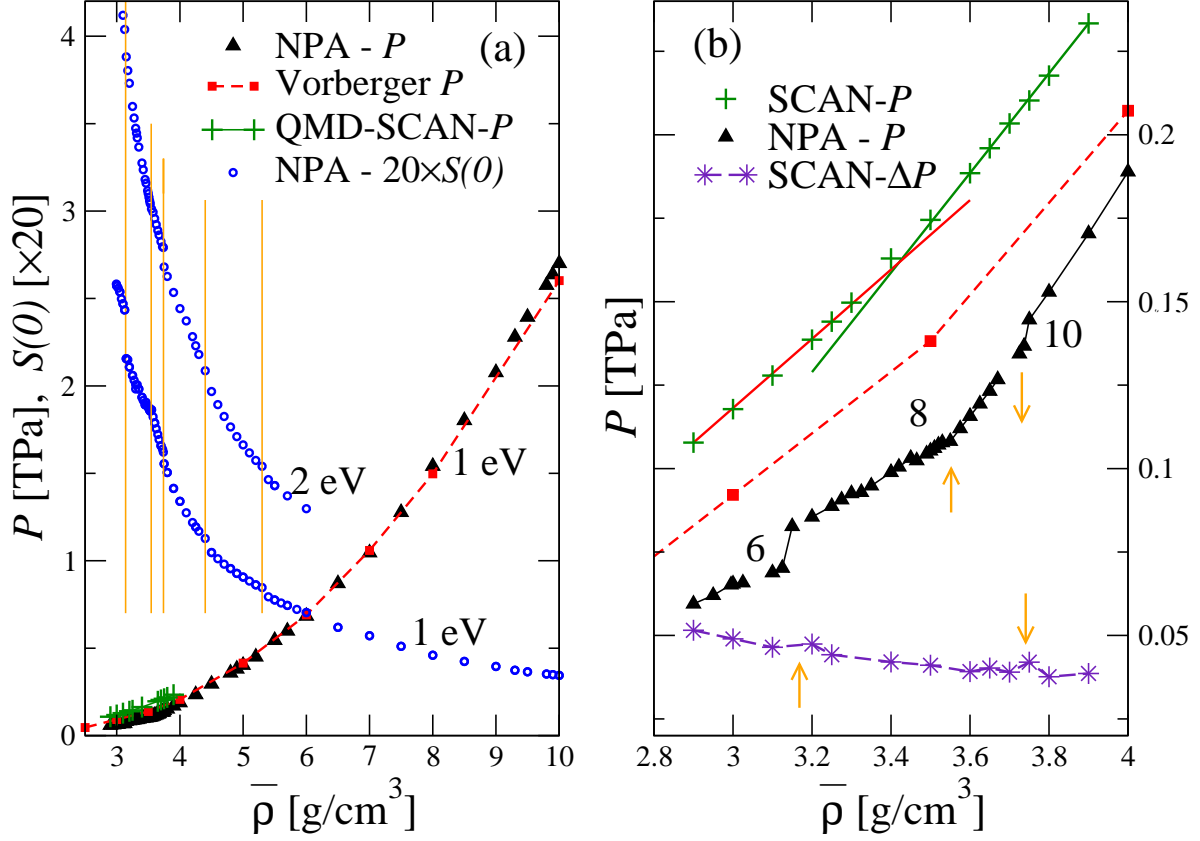


FIG. 4. (Color online) Evidence for LPTs in l -carbon from QMD and NPA calculations. (a) The pressure at 1 eV from QMD-PBE [5], QMD-SCAN and NPA calculations. The $k \rightarrow 0$ of $S(k)$, viz., $S(0) = \kappa/\kappa_0$ where κ is the isothermal compressibility. It displays discontinuities (vertical lines) at the LPTs. (b) The discontinuities in the range $2.9 \text{ g/cm}^3 < \bar{\rho} < 4 \text{ g/cm}^3$ from the NPA pressure indicate LPTs at $\bar{\rho} \sim 3.15 \text{ g/cm}^3$ (LPT₃), 3.52 g/cm^3 (LPT_{3.5}), 3.75 g/cm^3 (LPT_{3.7}). The data points above and below $\bar{\rho} \simeq 3.42 \text{ g/cm}^3$ from 108-atom QMD-SCAN simulations fall accurately on straight lines intersecting at $\bar{\rho} \simeq 3.42 \text{ g/cm}^3$ if a single Gaussian is fitted to the QMD P -distributions. However, the width of the SCAN-QMD P distributions (labeled SCAN- $\Delta P \times 3.3$) increases (arrows) at LPT₃ and LPT_{3.7} and are best fitted with two-Gaussians. See Fig. 5 for two densities near LPT₃.

energy calculation of the interacting system. Faussurier *et al* [30] have noted that the VASP code estimates the ionic contribution to the pressure using an ideal-gas approximation and a stress-tensor evaluation, rather than from the total free energy. This may also contribute to a difference between the QMD and NPA estimates of the pressure (where no ideal gas approximation is made). Furthermore, the NPA recovered the Ganesh-Widom pressure for

l-silicon close to its melt line accurately [8]. The Ganesh-Widom calculation implemented its own free energy calculation to obtain the pressure. So, the full power and rigour of QMD calculations may, or may not be available depending on how QMD codes implement the finite- T pressure calculations.

The discontinuities in P , and in $S(0)$ independently support one another. The behaviour of $S(0)$ at $T=2$ eV is also indicated in Fig. 4. The 1 eV pressure isotherm obtained from the QMD-scan calculation as well as that from the NPA are shown. The QMD results (obtained using the SCAN functional) independently confirm the LPTs found using the NPA, but at slightly shifted densities. Thus the NPA-LPT_{3.5} occurs at 3.42 g/cm³ in the QMD-SCAN data; this LPT corresponds to a structural adjustment when the form factor M_k changes sign (Fig. 1), while N_c remains at 8. The LPT_{4.5} is also a structural adjustment while N_c remains at 10. The origin of these LPTs is discussed in Sec. VI.

The QMD-SCAN pressure has a sharp break near the LPT_{3.5}. However, the other two LPTs seen in the NPA are not seen in the VASP pressure calculation. Whether this arises from unknown approximations in the NPA approach, or in the VASP calculation of the ionic contribution to P [30], or from the inadequate treatment of long-ranged effects (c.f., fig. 2) due to the finite-size of the simulation ($N = 108$) in QMD, is not clear.

However, a deeper examination reveals evidence of these two LPTs even in the QMD data. The pressure *fluctuations* ΔP are expected to form a Gaussian distribution (see Appendix) for a uniform equilibrated fluid (Fig. 5). The width ΔP in the QMD-SCAN (labeled SCAN- ΔP) changes significantly near the discontinuities (vertical arrows, Fig. 4(b)) at LPT₃ and LPT_{3.7}. They are best fitted to a sum of two Gaussians, (as seen in Fig. 5) unlike at LPT_{3.5}. The need for two-Gaussians at LPT₃ and LPT_{3.7} to describe the QMD pressure fluctuations provides some confirmation of the LPTs explicitly seen in the NPA calculation. However, phase transformations involve the cooperative action of large numbers of atoms, and hence we have also examined the N -dependence of the pressure estimates from the QMD simulations in the regime of densities where LPTs are found. This is discussed in the appendix and confirms that the $N=108$ QMD simulations probably provide converged values of the pressure.

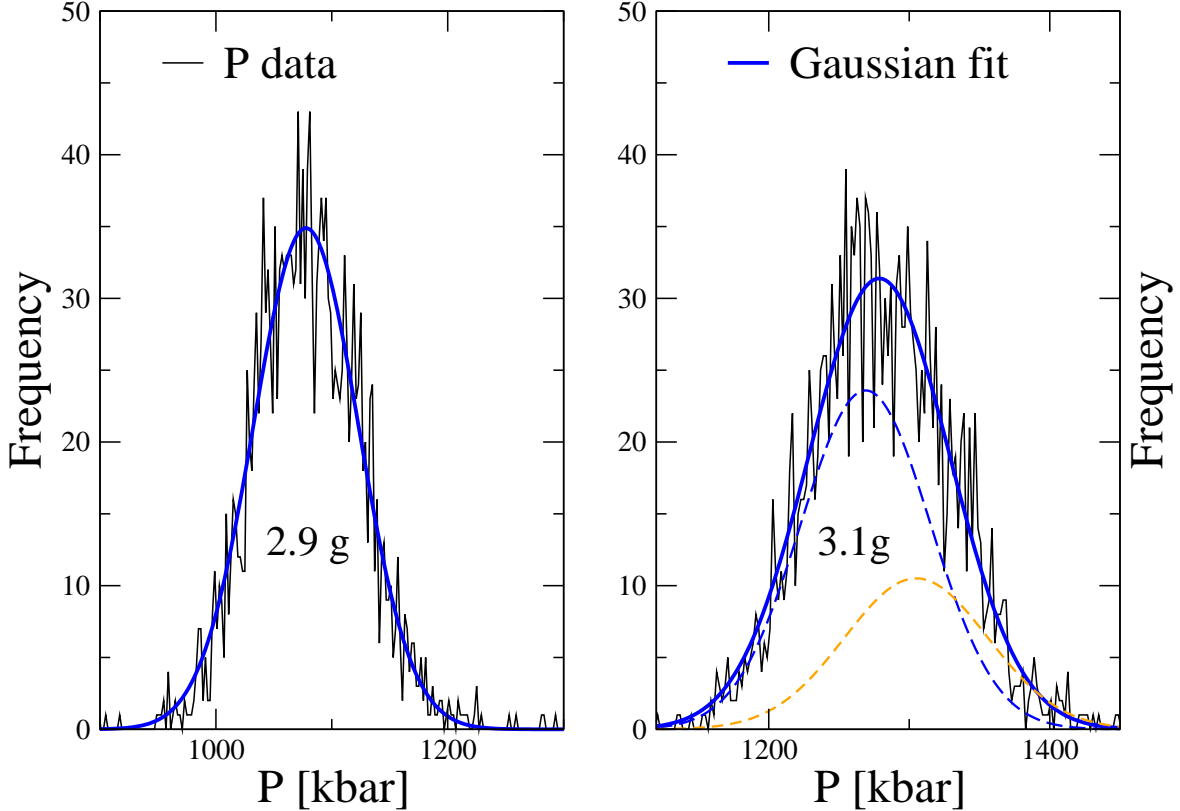


FIG. 5. (Colour online) The P -distribution from $N = 108$ atom QMD-SCAN calculations. (a) 2.9 g/cm^3 and (b) 3.1 g/cm^3 , at LPT_3 . While the 2.9 g/cm^3 case fits to one Gaussian, that at 3.1 g/cm^3 best fits to two Gaussians, implying an inhomogeneous system at the LPT in the 108-atom QMD simulation. The $\text{LPT}_{3.7}$ is also bimodal, but the $\text{LPT}_{3.5}$ is not bimodal (for more details, as well as results from $N = 64$ simulations, see the Appendix).

VI. THE ORIGIN OF DISCONTINUITIES IN THE NPA PRESSURE

Many average-atom (AA) models [31–35], also sometimes referred to as “atoms-in-jellium” models, confine all the bound and free electrons of an ion inside the Wigner Seitz sphere. This introduces an electron chemical potential different from the non-interacting chemical potential μ_0 required in density functional models. In DFT the interacting electrons are mapped onto a system of non-interacting electrons (i.e., μ_0 is applicable) at the *interacting* density. Thus AA models that use a $\mu \neq \mu_0$ are not strictly DFT models.

In the NPA the electrons are not confined to the WS-sphere, but to the correlation sphere which has a radius large enough to ensure that all pair-distribution functions have reached unity and all correlations have died out. Typically $R_c \sim 10r_{\text{ws}}$ to $5r_{\text{ws}}$ and μ_0 is the correct

chemical potential for the NPA, as required by DFT. Furthermore, simple AA models have to deal with electrons that “leak out” of the WS-sphere, and may produce model dependent effects arising from the choice of boundary conditions at the surface of the WS-sphere; these do not arise in the NPA.

However, NPA models as well as AA models have to deal with discontinuities that arise when a well-confined bound state moves upwards in energy and into the continuum due to changes in density or temperature. In some cases, such ionization is accompanied by phase transitions and discontinuities in physical properties [44]. In other cases, when unphysical discontinuities occur, they can be corrected by ensuring that appropriate discontinuities that cancel them are properly included in the xc-functionals. However, there are no changes in the degree of ionization (\bar{Z}) or any other critical parameters for l -carbon in the range of densities studied here, and hence no spurious discontinuities are expected in this range of $\bar{\rho}, T$.

The NPA pressure is obtained from an evaluation of the Helmholtz free energy F of the system. This consists of contributions of the form [21, 36]:

$$F = F_e^0 + F_e^{xc} + F_{em}^a + F_{em}^b + F_{12} + F_I^0. \quad (4)$$

The first two terms deal with the free energy of the non-interacting uniform electron fluid and its finite- T exchange-correlation energy at the given density and temperature T . The last term, F_I^0 is the ideal (classical) free energy of the ion subsystem. The third and fourth terms together form the embedding energy of the nucleus and the inhomogeneous electron density that form the neutral pseudo-atom in the uniform electron fluid. The fifth term, F_{12} contains the interactions between pseudoatoms brought in via the pair-potential, pair-distribution functions and the ion-ion correlation effects. The contribution to the pressure from all the terms except F_{12} can be expressed analytically. The density derivative of the term F_{12} has to be evaluated numerically to give a P_{12} . Then the pressure is:

$$P = P_e^0 + P_e^{ex} + P_{em}^a + P_{em}^b + P_{12} + P_I^0. \quad (5)$$

No discontinuities are expected in P_e^0, P_e^{ex} or P_I^0 when treated as a function of $\bar{\rho}$ as the number of free electrons per ion, \bar{Z} , remains constant at a value of four in this density range. Hence, in Fig. 6, panel (a) we display only the two components of the embedding pressure and the pair free energy F_{12} as a function of $\bar{\rho}$ at 1 eV.

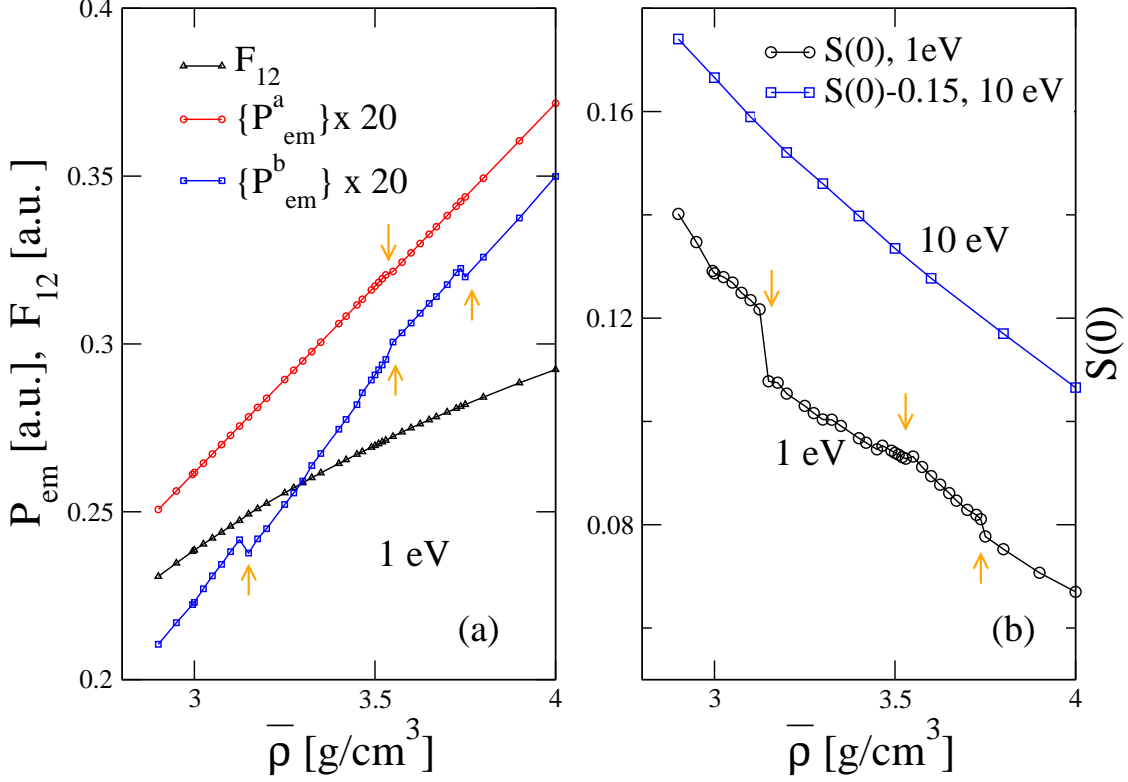


FIG. 6. (Color online) (a) The two components of the embedding pressure obtained (without numerical differentiation) from the embedding free energy of the neutral pseudo atom. The pair-interaction free energy F_{12} containing bonding effects is also displayed. The embedding pressure component P_{em}^b displays three discontinuities, while P_{em}^a shows a slight discontinuity near $\bar{\rho} = 3.52$. No discernible discontinuity is seen in the bonding free energy F_{12} , showing that the LPTs are not an effect associated with bonding or pair interactions. (b) The $k \rightarrow 0$ limit of the structure factor at 5 eV, 3 eV and 1 eV. $S(0) = \kappa/\kappa_0$, where κ_0, κ are the ideal fluid compressibility and the interacting compressibility respectively. The value of $S(0)$ at 5 eV is shifted by 0.09 and $S(0)$ at 3 eV by 0.08. $S(0)$ at 2 eV was displayed in Fig. 4.

In order to understand the physical content of the embedding pressure (see Ref. [36]) that contain the discontinuities, we define the symbol \star to define a convolution product. We also define the integration over all space via the symbol \circ . That is:

$$f \star g = \int f(\vec{r})g(\vec{r} - \vec{s})d\vec{s} \quad (6)$$

$$f \circ g = \int f(r)g(r)d\vec{r}. \quad (7)$$

The volume of integration is a sphere of radius $R_c \sim 10r_{ws}$ at low T and $\sim 5r_{ws}$ at higher T .

Then the potential that produces a single neutral pseudoatom in the uniform fluid of mean electron density \bar{n} and mean ion density $\bar{\rho}$, is:

$$V^{npa} = \frac{1}{r} \star (-Z\delta_0 + \nu + \Delta n). \quad (8)$$

Here $Z\delta_0$ defines the nuclear term at the origin, while ν (i.e., $\nu(r)$) is the density of the spherical cavity which mimics the ion distribution $\rho(r)$ by $\bar{Z}g_{cav}(r)$.

$$\nu(r) = \bar{n}, r > r_{ws}, \text{ else } \nu(r) = 0. \quad (9)$$

Also, Δn is the displaced electron density with reference to the mean electron density \bar{n} . Then, denoting the volume of the Wigner-Seitz sphere by Ω_{ws} , the two embedding pressures can be written as [36]:

$$P_{em}^a = (\nu - \bar{n}) \circ V^{npa} / \Omega_{ws} \quad (10)$$

$$P_{em}^b = -\bar{Z}V^{npa}(r_{ws}). \quad (11)$$

Since $\bar{Z} = 4$, and remains at that value through out the range of densities studied, the discontinuities in the embedding pressure are caused solely by the ‘external potential’ associated with the creation of the carbon pseudoatom and its pseudopotential (c.f., Fig. 1).

This re-enforces our conclusion that the observed LPTs are associated with changes in coordination number N_c and the effect on the electron-ion interactions at the Fermi energy via $q = 2k_F$ scattering. The coordination number N_c can be approximately determined from the area under the first peak of $g(r)$, and has been reported in detail by Vorberger *et al* [5]. Changes in N_c do not seem to appear as discontinuities in QMD P but clearly cause discontinuities in the NPA pressure and the NPA compressibility i.e., a derivative of the pressure which is independently calculated via $S(0)$. The long range of the NPA potentials seems to play a significant role here.

The role of the long-ranged Friedel oscillations in “ordering the fluid” is made clearer by an examination of the potentials in the density ranges below ρ_D , near $\rho_D = 3.5 \text{ g/cm}^3$ and above ρ_D . These are provided in Fig. 7 which is discussed below.

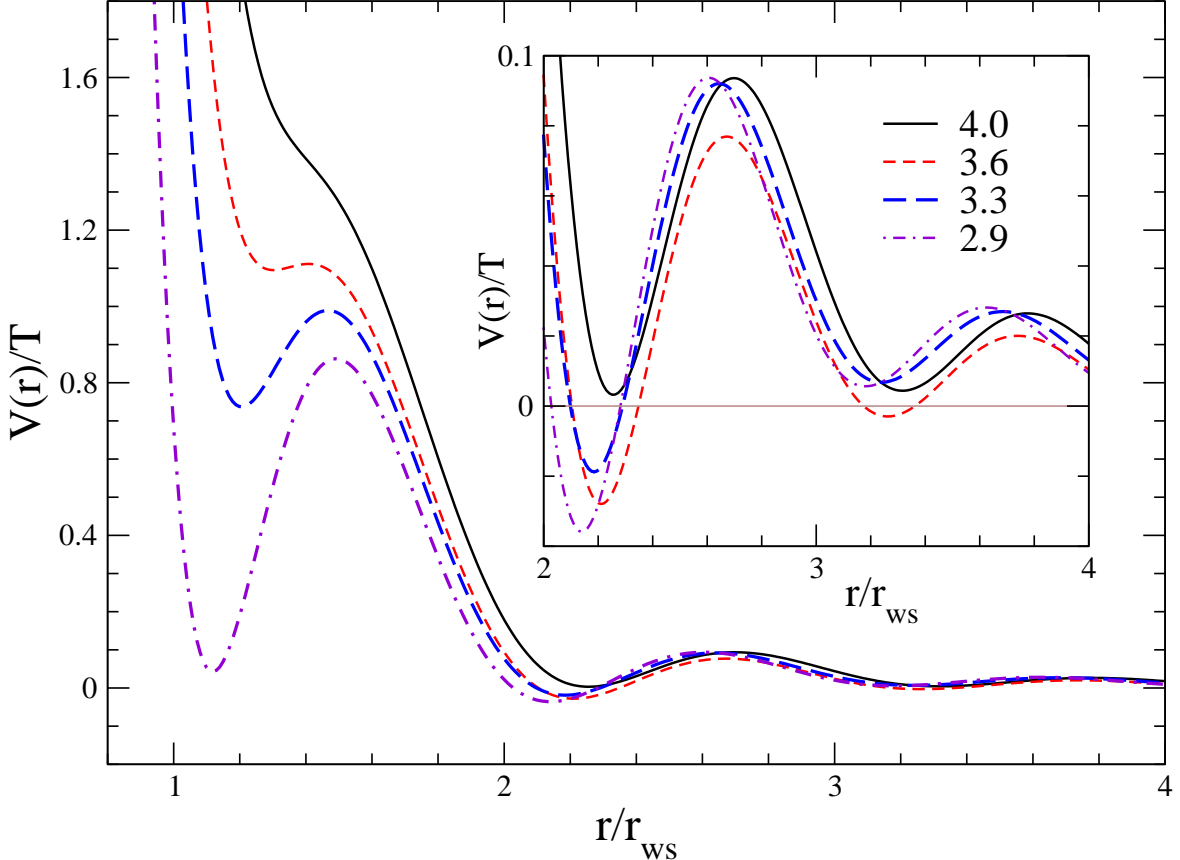


FIG. 7. (Color online) C-C pair potentials at densities in regions separated by the discontinuities in the pressure. The densities shown (4, 3.6, 3.3, 2.9 g/cm³) are for regions where the coordination numbers $N_c \sim 10, 8, 6$, and $N_C < 6$ prevail. The discontinuities imply LPTs in the NPA calculation. The QMD data show a discontinuity near the the diamond density, but only broadenings in the pressure fluctuations at the other LPTs, as displayed in Fig. 5.

VII. DISCUSSION

The structure factor data show that the structure of *l*-carbon is determined by strong electron-ion scattering across the Fermi surface, and by the Friedel oscillations of the pair-potentials acting in consort to produce a subsidiary peak in $S(k)$ at twice the Fermi wavevector. This ‘Coulomb fluid’ model of *l*-carbon provides a complete account of the structural and thermodynamic properties of *l*-carbon and its liquid-liquid phase transitions without invoking covalent bonds, using only simple *s*-wave pair-potentials. The covalent bonds are mere transients, lasting the lifetime of longitudinal phonons, while DFT deals with thermodynamic ($\omega \rightarrow 0$) averages.

The LPT_{3.5} near $\bar{\rho}_D$ is evident in the QMD-SCAN P data that accurately fall on two straight lines crossing at 3.42 g/cm³. The LPT occurs almost at the nominal ‘diamond’ density, when $U_{ei}(2k_F)$ becomes zero thereby creating a strong ion-ion interaction. A discontinuity in the electrical conductivity is also found at this density (see the last figure in the Appendix).

The minima in the pair potential $V(r)$ (see Fig. 7) are all positive in the high density region (e.g., $\bar{\rho} = 4$ g/cm³), with $N_c \sim 10$ or more. The next lower density region develops a deeper first minimum and negative secondary minima. The third region (e.g., $\bar{\rho} = 3.3$ g/cm³) pulls in ions to the center by making the secondary minima less attractive. In the lowest density region the first minimum becomes deep, and eventually becomes negative enough (e.g, exceeds twice the thermal energy) to form persistent covalent bonding.

The NPA calculation is for a uniform fluid where the $2k_F$ scattering is tightly linked to the liquid structure and the coordination number through the Friedel minima in the pair potential. They correlate the whole fluid as in a charge-density wave that could have existed in a solid. It is this tight coupling of the ionic structure to the Friedel oscillations that lead to LPTs at each change of coordination number, a phenomenon common to l -Si [8]. Previous studies of LPTs [12, 14] using QMD, by the very nature of its methodology emphasized real-space short-ranged chemical bonding (e.g., $sp^3 \rightarrow sp^2$) with short life times and did not address the physics of $2k_F$ scattering and related ‘Fermi-liquid’ phenomena.

In conclusion, the ionic and electronic structure of l -carbon can be accurately and inexpensively modeled as that of a uniform *liquid metal* whose structure is dominated by strong electron-ion interactions at the Fermi surface. We find three liquid-liquid phase transition at 1 eV in the range 2.9-4.0 g/cm³ confirmed by both NPA and QMD calculations, and two higher-density LPTs. These results and similar results for l -Si [8] suggest that metallic fluids with a peak in $S(k)$ at $2k_F$ are strongly Friedel correlated liquids that display multiple LPTs.

Our conclusion that l -carbon is a ‘good metal’ is of interest to long-standing controversies regarding the magnetism of giant planets [37] and also white dwarfs [38]. Hence these results for carbon are relevant to terrestrial as well as astrophysical systems, and critical to emerging carbon materials [1].

DATA AVAILABILITY

All the data used in this paper are available within the article in graphical form in the figures 1 to 10. If there is any difficulty in extracting them from the figures, the data can be provided on request from the authors.

Appendix

This Appendix addresses the following topics:

- Details of the two density functional methods (namely, QMD and NPA methods) used here and results for $N = 108$ and $N=64$ simulations.
- The NPA pseudopotentials and pair-potentials.
- Non-subjective estimation of the pressure from QMD runs and evidence to support the existence of a more broadened type of pressure distribution at liquid-liquid phase transitions LPT_3 and $LPT_{3.7}$.
- The electrical conductivity of liquid carbon.

1. Details of the two density functional methods

The theoretical methods used in this study are (a) one-atom DFT as implemented in the NPA, and (b) many-atom DFT (QMD) simulations using $N=108$ and $N=64$ carbon ions and the associated number of electrons assuming two bound electrons per ion. The NPA is an ‘all-electron’ method while the QMD used here employed a pseudopotential and hence the 108 ion simulation included 432 electrons, while the $N = 64$ included 256 electrons.

2. The QMD simulations

These are finite- T DFT-MD (QMD) calculations where classical molecular dynamics is used to evolve 108 ions in a cubic simulation cell, while the electrons, with four ionized

TABLE I. The pressure in kB at 1 eV obtained from QMD calculations using $N = 64$ and $N = 108$ carbon ions in the simulation.

$\bar{\rho}$, g/cm ³	3.0	3.1	3.2	3.3	3.6	3.7	3.8	3.9
P , $N = 64$, kB	1182	1277	1383	1500	1887	2030	2182	2338
P , $N = 108$, kB	1178	1279	1386	1506	1885	2034	2177	2334

electrons per carbon atom are treated quantum mechanically using density functional theory. The numerical code implemented in the Vienna ab initio simulation package VASP 5.4.4 [17], and the projector augmented-wave pseudopotential for the interaction between the nuclei and the electrons provided in VASP were used. The exchange and correlation potential is approximated by the SCAN functional which has been found to perform better for systems with covalent interactions [19]. The simulations used an energy cutoff of 414 eV and a simulation time of 4 ps. The ion temperature was controlled with a Nosé thermostat, and enough empty bands were included to ensure that the highest energy bands had negligible occupations. Evaluations of the Brillouin zone were performed at the Baldereschi k -point [39].

The pressure obtained by the $N = 64$ and 108 calculations are given in Table I for typical densities used in the main study. These pressure values suggest that the $N = 108$ simulation is adequately converged for our purposes. The pressure at the lower densities fall onto a straight line, while those at the higher densities fall on a different straight line, with the pressure discontinuity occurring at the critical concentration $\rho_{cr} = 3.40$ g/cm³ for $N = 64$, while the $N = 108$ data place the discontinuity at 3.42 g/cm³ (see Fig. 4). The simulation box size varies as $N^{1/3}$. Extrapolation of the two values of ρ_{cr} as a function of $1/N^{1/3}$ gives the large- N limit to be 3.524g/cm³, consistent with the NPA estimate of $\rho_{cr}=3.52$ g/cm³.

3. The NPA calculations

For a fluid, these are essentially like a self-consistent atomic structure calculation for a single nucleus placed in averaged-out spherically symmetric electronic and ionic densities, and have strong similarities to an average-atom calculation [31–35]. The environment

is described by one-body densities $n(r)$ of electrons, and $\rho(r)$ of ions, rather than by explicitly enumerated atoms (as used in QMD). The one-body densities $n(r)$ and $\rho(r)$ are self-consistently evaluated using Kohn-Sham type finite- T DFT equations. In addition to the quantum Kohn-Sham equation derived from the stationary condition on the grand potential $\Omega([n], [\rho])$ for functional derivation with respect to the electron density $n(r)$, we use the stationary condition for variations of the ion density as well. Thus,

$$\delta\Omega(n, \rho)/\delta\rho = 0 \tag{A.1}$$

is used in the theory of the NPA method. This involves an ion-ion xc-functional where the exchange part is zero since the ions can be treated as classical particles in most cases. Furthermore, instead of the Kohn-Sham equation, we get a classical DFT equation [40, 41] that can be identified as a Boltzmann-like distribution for $\rho(r)$ that has to be solved simultaneously with the Kohn-Sham equation [25] for the electron density $n(r)$. This can be done either using MD, or using an integral equation approach exploiting the spherical symmetry of the fluid.

$$\rho(r) = \bar{\rho} \exp\{-V_{\text{cKS}}(r)\}. \tag{A.2}$$

The classical Kohn-Sham potential $V_{\text{cKS}}(r)$ occurring in the above equation can be identified with the potential of mean force used in the theory of liquids. Then the ion-ion xc-potential can be seen to equal to the sum of hyper-netted-chain diagrams and bridge diagrams, if the electron-ion xc-potential is neglected [25]. The electron-ion xc-functional F_{ei}^{xc} is usually neglected in most NPA calculations, being largely equivalent to making the Born-Oppenheimer approximation, and neglecting certain correlation corrections of the form $\langle n(\mathbf{r})\rho(\mathbf{r}') \rangle - \langle n(r) \rangle \langle \rho(r') \rangle$. This is equivalent to using a ‘random-phase type’ approximation for the electron-ion response function in regimes where we have already used the linear-response form for the electron response. This neglect of F_{ei}^{xc} is quite appropriate for dense uniform fluids of carbon studied here.

The bridge contributions can be included using the hard-sphere model, with the hard sphere packing fraction parameter η selected using the Lado-Foils-Ashcroft criterion [42]. We find that the inclusion of bridge corrections has only a negligible effect for the calculation of the pressure or the compressibility of l -carbon in the range of $\bar{\rho}, T$ studied here, unlike for l -aluminum. Typical values are given below. For any given case, the whole calculation including the evaluation of pair-potentials, structure factors, pressure, compress-

TABLE II. . The NPA pressure at 1 eV without (labeled no B) and with (labeled with B) bridge corrections, and the corresponding hard-sphere packing fraction η for selected densities.

ρ g/cm ³	3.0	4.0	8.0
P TPa, no B	0.03413	0.1705	1.540
P TPa, with B	0.03359	0.1700	1.538
η	0.1080	0.2030	0.3515

ibilities, electrical and thermal conductivities can be carried out on a small laptop within a few minutes of computational time. The small- k limit of $S(k)$ is directly available from these calculations, unlike in QMD calculations where the finite-size L of the simulation box limits the smallest available k value to $\sim \pi/L$. An HP-folio9470m laptop has been used for NPA computations. Calculations for over 60 densities each were carried out on isotherms of 1 eV, 2 eV, etc., while somewhat fewer densities were studied at 0.8 eV, 3 eV, 5 eV and 10 eV. A sample of those results are presented here.

Detailed discussions of the NPA may be found in several recent publications [8, 16], as well as in some of the earlier publications [21, 25, 36]. In this study, the density $\bar{\rho}$, and temperature T (in energy units) are such that the carbon atom carries only the $1s$ shell of bound electrons, providing a very simple model of an atom in its electronic and ionic environment, and the corresponding NPA equations are discussed in detail in Ref. [10]. The notation of the presentation as well as the procedures used in the NPA method deployed here are identical and hence the reader is referred to that publication.

4. The NPA pseudopotentials and pair potentials

The pseudopotentials and pair potentials have been constructed using a linear response (LR) approximation. The KS calculation for the electron states for the NPA in a fluid involves solving a simple radial equation. The continuum states $\phi_{k,l}(r), \epsilon_k = k^2/2$, with occupation numbers f_{kl} , are evaluated to a sufficiently large energy cutoff and for an appropriate number of l -states (typically 9 to 39 were found sufficient for the calculations presented here). The very high- k contributions are included by a Thomas-Fermi correction.

This leads to an evaluation of the free-electron density $n_f(r)$, and the free-electron density pileup $\Delta n'(r) = n_f(r) - \bar{n}$. A part of this pileup is due to the presence of the cavity potential. This contribution $m(r)$ is evaluated using its linear response to the electron gas of density \bar{n} using the interacting electron response $\chi(q, T_e)$. The cavity corrected free-electron pileup $\Delta n_f(r) = \Delta n'(r) - m(r)$ is used in constructing the electron-ion pseudopotential as well as the ion-ion pair potential $V_{ii}(r)$ according to the following equations (in Hartree atomic units), given for Fourier-transformed quantities:

$$U_{ei}(k) = \Delta n_f(k) / \chi(k, T_e), \quad (\text{A.3})$$

$$\chi(k, T_e) = \frac{\chi_0(k, T_e)}{1 - V_k(1 - G_k)\chi_0(k, T_e)}, \quad (\text{A.4})$$

$$G_k = (1 - \kappa_0/\kappa)(k/k_{\text{TF}}); \quad V_k = 4\pi/k^2, \quad (\text{A.5})$$

$$k_{\text{TF}} = \{4/(\pi\alpha r_s)\}^{1/2}; \quad \alpha = (4/9\pi)^{1/3}, \quad (\text{A.6})$$

$$V_{ii}(k) = Z^2 V_k + |U_{ei}(k)|^2 \chi_{ee}(k, T_e). \quad (\text{A.7})$$

Here χ_0 is the finite- T Lindhard function, V_k is the bare Coulomb potential, and G_k is a local-field correction (LFC). The finite- T compressibility sum rule for electrons is satisfied since κ_0 and κ are the non-interacting and interacting electron compressibilities respectively, with κ matched to the $F_{xc}(T)$ used in the KS calculation. In Eq. A.6, k_{TF} appearing in the LFC is the Thomas-Fermi wavevector. We use a G_k evaluated at $k \rightarrow 0$ for all k instead of the more general k -dependent form (e.g., Eq. 50 in Ref. [27]) since the k -dispersion in G_k has negligible effect for the WDMs of this study. The xc-functional is used in the LDA which is efficient and accurate because the one-center electron density $n(r)$ is smooth compared to the complex N -center electron density used in VASP-type N -center DFT calculations.

Unlike Si^{4+} with a robust core, the C^{4+} ion produces strong interactions, especially in the low- $\bar{\rho}$, low- T region. Stanek *et al* [16] showed that linear-response (LR) potentials generated from NPA for l -C at the ‘‘graphite density’’ $\rho_{\text{G}} \simeq 2.267 \text{ g/cm}^3$ at low T strongly overestimated the first peak of the ion-ion pair distribution function (PDF) $g(r)$. LR is known to fail for expanded metals at low T and here we only study densities $\bar{\rho} > 2.9 \text{ g/cm}^3$.

On the other hand, QMD calculations with smaller N lead to pair-potentials where the long-ranged Friedel oscillations are not accurately implemented (see Fig. 2, and Ref. [44]). While this may not be too important in many liquid metals, they may be crucial to l -carbon and kindred materials where a $2k_F$ subpeak occurs in the structure factor and enforces a high degree of ordering in k -space.

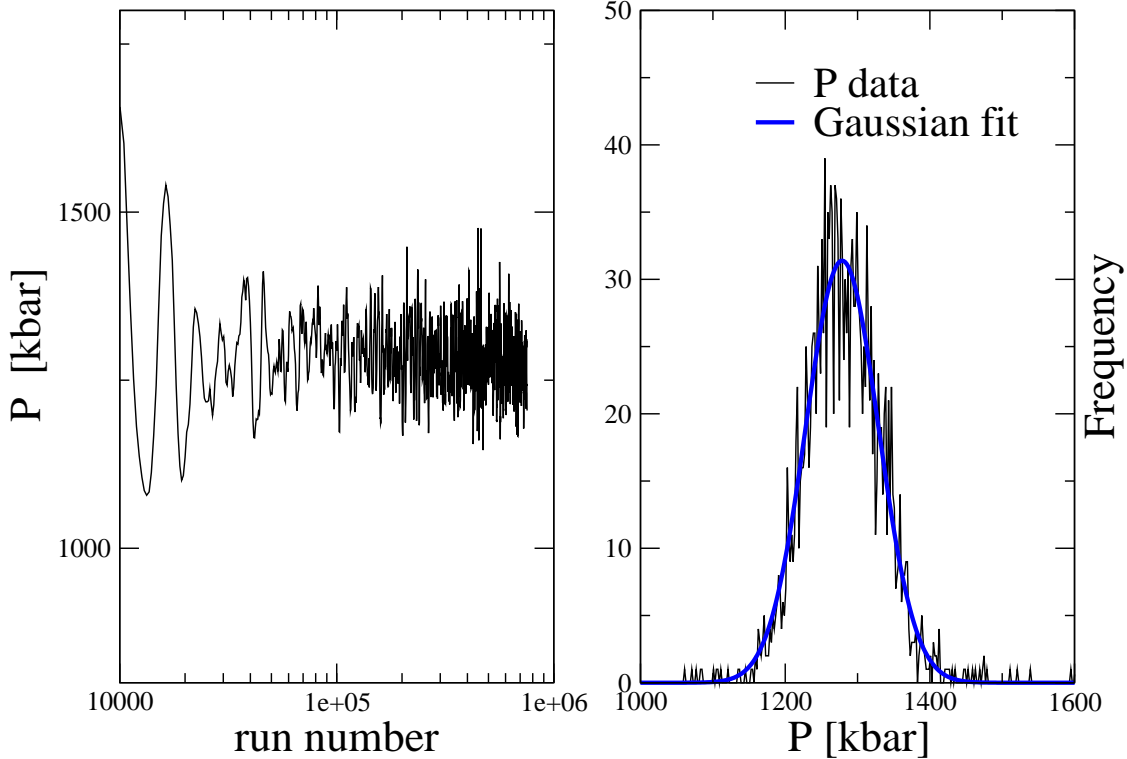


FIG. 8. (Color online) (Left Panel) Pressure ‘readings’ at 1 eV from a DFT-MD simulation using 108 atoms at 3.1 g/cm^3 on the low density side prior to the LPT_3 . The ‘run number’ is an arbitrary index. (Right panel) The pressure ‘readings’ are fitted to a Gaussian (unnormalized), and the equilibrium pressure is taken to be that corresponding to the maximum of the Gaussian. In the present case a bimodal character is clear and a sum of two Gaussians with weights of 0.699 and 0.301 is appropriate.

5. The Gaussian distributions for QMD-SCAN estimates of the equilibrium pressure.

Since the evidence for the LPTs are to be based on breaks in the predicted pressure, particular care was used to determine the equilibrium pressure from the simulation in a consistent, non-subjective manner. The QMD simulation records a distribution of pressures around the thermodynamic mean value, and they form a Gaussian distribution for a *uniform fluid* at equilibrium. We expect the Gaussian to be more narrow when the number of atoms N in the QMD simulation is increased. Hence we show the distributions for $N=108$ and $N = 64$ ins several cases.

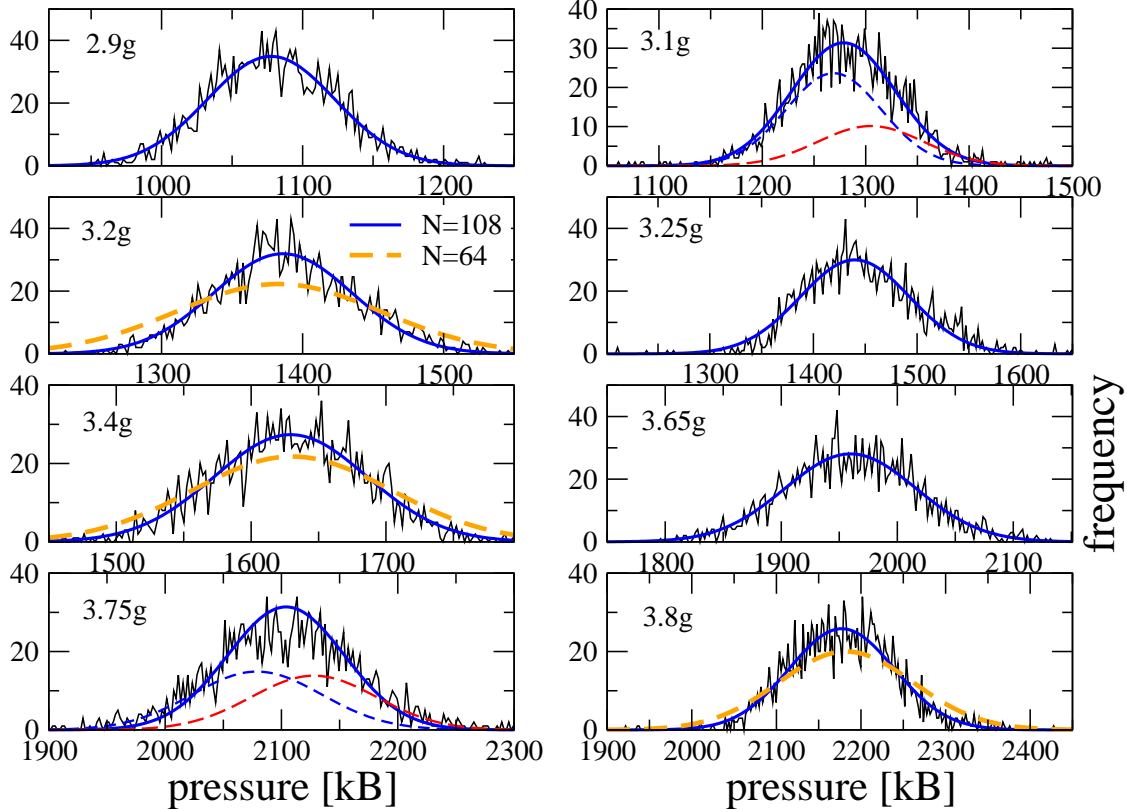


FIG. 9. (Color online) Pressure ‘distributions’ at 1 eV fitted to Gaussians. The distributions at $\bar{\rho}=3.1$ g/cm³ (see LPT₃), Fig.4 and $\bar{\rho}=3.75$ g/cm³ (LPT_{3.7}) are broader and use a two-Gaussian fit. Although there is a discontinuity in the QMD-SCAN pressure at 3.42 g/cm³ (LPT_{3.5}, the P distribution at 3.4 g/cm³ shows no clear tendency to a bimodal distribution. The $N = 64$ distributions are also shown for the densities 3.2, 3.4 and 3.8 g/cm³.

Hence the simulation data were fitted to a Gaussian form and the most probable pressure was determined from the peak of the Gaussian. Very close to a phase transition, relevant physical quantities show larger fluctuations. They may not show a unique value and become ill-defined. In two cases, viz., near the LPT₃ and LPT_{3.7}, an average over two Gaussians seemed more appropriate.

The pressure evaluated in this manner, using the SCAN xc-functional is plotted as SCAN- P in Fig. 4(b) of the main text. The width of the unnormalized Gaussian distribution, ΔP is used to characterize the density fluctuations in the system and are displayed in panel (b) of Fig. 4 of the main text, and labeled SCAN- ΔP . Using the fit form $f(p) = a \exp\{-w^2(p - p_m)^2\}$ for the frequency of occurrence of the pressure, p_m is the

mean pressure, while w was taken as a measure of the width of the distribution. The width has been multiplied by a factor of 3.3 in order to plot it in the same range as the other curves.

It should be appreciated that the pressure, a thermodynamic property, is effectively undefined exactly at the discontinuity. Close to a phase transition, if a simulation with a finite number N of particles is carried out, the width of the data narrows as N approaches the thermodynamic limit. The existence of two peaks in the distribution does not mean that there are ‘two’ thermodynamic pressures, but merely a property of the smaller N simulation and the effect of density fluctuations near a phase transition when fluctuations between two possible fluid states become possible. We have used simulations at $N = 64$ and $N = 108$. However, statistical effects scale only as $1/\sqrt{N}$, and further study is warranted in future investigations.

6. The static electrical conductivity σ

The static conductivity of l -carbon has been a matter of long-standing concern in regard to the magnetism of giant planets [37] and in white dwarfs [38]. The conductivity usually changes at phase transitions because at least one of several physical parameters change abruptly. These are, e.g., the number of free carriers, the distribution of the ions that cause the scattering of electrons, and the scattering potential. These properties are contained in the pseudopotential $U_{ei}(k)$, the structure factor $S(k)$ and the screening function of the system, when considering the static conductivity.

In the present case \bar{Z} remains unchanged at four. The high value of the Fermi energy E_F of liquid carbon, e.g., 28.8 eV near the diamond density of 3.5 g/cm³, implies that at 1 eV the electrons are nearly completely degenerate, and hence electron scattering can occur only from one edge of the Fermi surface to the other, with a momentum transfer $q = 2k_F$, where k_F is the Fermi momentum. Thus the quantities $U_{ei}(2k_F)$, $S(2k_F)$ and the inverse dielectric function at $2k_F$ which screens the pseudopotential are the physical quantities that determine the electrical conductivity.

We noted that, due to the strong electron-ion scattering at $2k_F$, the structure factor remains tied to a peak at $2k_F$. Thus sharp changes are NOT expected in the electrical conductivity of this system at liquid-liquid phase transitions. However, an extremely weak

discontinuity can be seen (Fig. 10) at the LPT_{3.5}, i.e., at the nominal diamond density. Here we also noted a discontinuity in the pressure calculated via QMD-SCAN, and via the NPA model, corresponding the reduction of the form factor of the pseudopotential at $2k_F$ to zero at this density. Given the very small magnitude of the discontinuity in σ at LPT_{3.5}, it is not surprising that no discontinuities in σ are seen at LPT₃ and LPT_{3.7} where the QMD pressure isotherm also did not show any discontinuities.

The electrical conductivity estimate by Vorgerber *et al* [5], using the PBE-functional and the Kubo-Greenwood (KG) formula is also given, and reports a lower conductivity. The static conductivity is estimated from the dynamic conductivity of the KG calculation by an extrapolation to the static limit and averaged over. The use of a Drude form for this extrapolation is often used in spite of the importance of transient bonds in these systems. It is known that the theoretical predictions and experimental data when available (e.g., for *l*-silicon) are only in qualitative agreement [8] for these metallic transiently bonded fluids.

-
- [1] C. J. Hull, S. L. Raj, and R. J. Saykally, *Chemical Physics Letters* **749**, 137341 (2020).
 - [2] A. Lazicki, D. McGonegle, J. R. Rygg, D. G. Braun, D. C. Swift, M. G. Gorman, R. F. Smith, P. G. Heighway, A. Higginbotham, M. J. Suggit, D. E. Fratanduono, F. Coppari, C. E. Wehrenberg, R. G. Kraus, D. Erskine, J. V. Bernier, J. M. McNaney, R. E. Rudd, G. W. Collins, J. H. Eggert and J. S. Wark, *Nature* **589**, 532 (2021).
 - [3] G. Galli, R. Martin, R. Car, and M. Parrinello, *Phys.Rev. Lett.* **63**, 988 (1989).
 - [4] Lorin X Benedict, Kevin P Driver, Sebastien Hamel, Burkhard Militzer, Tingting Qi, Alfredo A Correa, A Saul, Eric Schwegler, *Phys. Rev. B* **22** 224109 (2014).
 - [5] J. Vorberger, K. U. Plageman, and R. Redmer, *High Energy Density Physics* **35**, 100737 (2020).
 - [6] M. W. C. Dharma-wardana, and F. Perrot, *Phys. Rev. Lett.*, **65**, 76 (1990).
 - [7] P. Ganesh, P. and M. Widom, *Phys. Rev. Lett.* **102**, 075701 (2009).
 - [8] M. W. C. Dharma-wardana, Denis. D. Klug, and R. C. Remsing, *Phys. Rev. Lett.* **125**, 075702 (2020).
 - [9] H. Zong, V. N. Robinson, A. Hermann, and L. Zhao *Nature Physics*, **17**, 955 (2021).
 - [10] M. W. C. Dharma-wardana, *Phys. Rev. E* **104**, 015201 (2021).

- [11] M. V. Thiel, and F. H. Ree, Phys. Rev. B **48**, 3591 (1993).
- [12] J. N. Glosli, and F. H. Ree, Phys. Rev. Lett. **82**, 4659 (1999).
- [13] J. P. Perdew, K. Burke, K., and M. Ernzerhof, Phys. Rev. Lett. **77**, 3865 (1996).
- [14] C. J. Wu, J. N. Glosli, G. Galli, and F. H. Ree, Phys. Rev. Lett. **89**, 135701 (2002).
- [15] D. Kraus, D., J. Vorberger, D. O. Gericke, V. Bagnoud, A. Blazevic, W. Cayzac, A. Frank, G. Gregori, A. Ortner, A. Otten, F. Roth, G. Schaumann, D. Schumacher, K. Siegenthaler, F. Wagner, K. Wunsch, and M. Roth, Phys. Rev. Lett. **111**, 255501 (2013).
- [16] Lucas J. Stanek, Raymond C. Clay III, M. W. C. Dharma-wardana, Mitchell A. Wood, Kristian R. C. Beckwith, and Michael S. Murillo, Phys. Plasmas **28**, 032706 (2021).
- [17] G. Kresse, G. and Furthmüller, J. Phys. Rev. B **54**, 11169 (1996).
- [18] X.Gonze, B. Amadon, G. Antonius, F. Arnardi, Lucas Baguet, Jean-Michel Beuken, Jordan Bieder, F. Bottin, Johann Bouchet, Eric Bousquet, *et al*, Computer Physics Communications, **248**, 107042 (2020).
- [19] R. C. Remsing, M. L. Klein, and J. Sun, Physical Review B **96** 024203 (2017).
- [20] J. Sun, B. Xiao, Y. Fang, R. Haunschild, P. Hao, A. Ruzsinszky, G. I. Csonka, G. E. Scuseria, and J. P. Perdew, Phys. Rev. Lett. **111**, 106401 (2013).
- [21] F. Perrot, and M. W. C. Dharma-wardana, Phys. Rev. E. **52**, 5352 (1995).
- [22] M. W. C. Dharma-wardana, Proceedings of the Conference on Density Functional Theory, Debrecen, 2015. Edited by K. Schwarz and A. Nagy. *Computation* **4** (2), 16; 2016,
- [23] L Harbour, and G. D. Förster, M. W. C. Dharma-wardana and Laurent J.Lewis, Physical review E **97**,043210 (2018).
- [24] H. D. Whitley, D. M. Sanchez , S. Hamel , A. A. Correa, and L. X. Benedict, Contrib. Plasma Phys. **55**, 390 (2015).
- [25] M. W. C. Dharma-wardana, and F. Perrot, Phys. Rev. A **26**, 2096 (1982).
- [26] G.C. Aers, M.W.C. Dharma-wardana and M. Gibb, Phys. Rev. B **33**, 4307 (1986). [NRCC 25290]
- [27] F. Perrot, and M. W. C. Dharma-wardana, Phys. Rev. B **62**, 16536 (2000); *Erratum:* **67**, 79901 (2003).
- [28] T. Dornheim, G. Groth, G. and B. Bonitz, Physics Reports, **744**, 1-86 (2018).
- [29] M. W. C. Dharma-wardana, Phys. Rev. B **100**, 155143 (2019).
- [30] G. Faussurier, C. Blancard, and M. Bethkenhagen, CPhys. Rev. E **104**, 025209 (2021).

- [31] J. A. Anta and A. A. Louis, Phys. Rev. B **61**, 11400 (2000).
- [32] M. S. Murillo, J. Weisheit, S. B. Hansen, and M. W. C. Dharma-wardana, Phys. Rev. E **87**, 063113 (2013).
- [33] Balas F. Rosznyi, High Energy Density Physics **4** 64 (2008)
- [34] C. E. Starrett, D. Saumon, J. Daligault, and S. Hamel, Phys. Rev. E **90**, 033110 (2014).
- [35] Yong Hou, Yongsheng Fu, Richard Bredow, Dongdong Kang, Ronald Redmer, Jianmin Yuan, High Energy density Physics **22** 21 (2017).
- [36] F. Perrot, Phys. Rev. E **47**, 570 (1993).
- [37] M. Ross, Nature **292** 475 (1981).
- [38] P. Dufour, J. Liebert, G. Fontaine, N. Behara, Nature **450**, 522 (2007).
- [39] A. Baldereschi, Phys. Rev. B, **7**, 5212 (1973).
- [40] J. Chihara, Progr. Theor. Phys. Jpn. **59**, 1085 (1978).
- [41] R. Evans, Adv. Phys. **28**, 143 (1979).
- [42] F. Lado, S. M. Foiles, and N. W. Ashcroft, Phys. Rev. **A** **26**, 2374 (1983).
- [43] M. W. C. Dharma-wardana, Physics of Plasmas **28**, 052108 (2021).
- [44] M. W. C. Dharma-wardana, Contrib. Plasma Phys. **58**, 128-142 (2018).

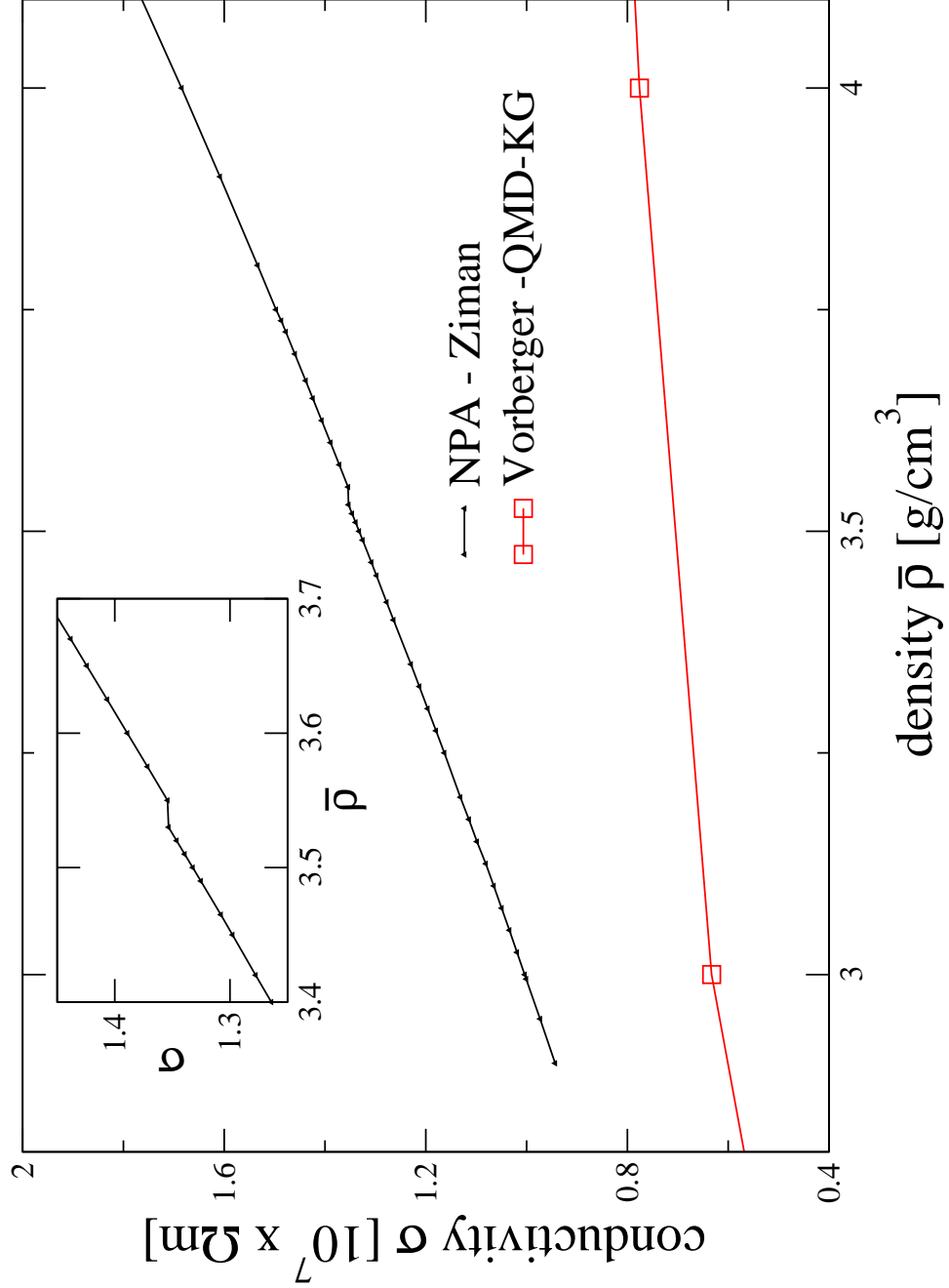


FIG. 10. (Color online) The conductivity calculated using the NPA pseudopotential $U_{ei}(k)$ and the structure factor $S(k)$ in the Ziman formula is displayed. The conductivity results reported by Vorberger *et al* is also displayed. The slight discontinuity in σ at $\simeq 3.53$ g/cm³ is shown in more detail in the inset. The discontinuity coincides with the LPT_{3.5}. The conductivity shows no discernible discontinuities at the other two LPT_{3.1}.